Nuclear Physics A397 (1983) 313–342

ANGULAR-MOMENTUM TRANSFER AND ALIGNMENT IN DEEP-INELASTIC REACTIONS FOR NEARLY SYMMETRIC HEAVY-ION SYSTEMS

A. J. PACHECO†, G. J. WOZNIAK, R. J. McDONALD, R. M. DIAMOND, C. C. HSU††, L. G. MORETTO, D. J. MORRISSEY,††† L. G. SOBOTKA and F. S. STEPHENS

Nuclear Science Division, Lawrence Berkeley Laboratory, University of California, Berkeley, CA 94720, USA

Received 8 September 1982

Abstract: The magnitude and alignment of the spin transferred to the fragments in the deep-inelastic reactions of 8.5 MeV/nucleon ^{165}Ho on ^{176}Yb, ^{148}Sm, and ^{nat}Ag were investigated using continuum γ-ray multiplicity and anisotropy techniques. The detection system consisted of a highly redundant arrangement of particle and γ-ray detectors and a γ-ray multiplicity filter. By using suitable reduced quantities, we show that for the most negative Q-values the multiplicity data are consistent with rigid-rotation of the intermediate dinuclear complex. The anisotropy data are compared to an equilibrium statistical model calculation. The sensitivity of the calculation to different assumptions concerning the composition of the γ-ray spectra is investigated. The magnitude and alignment of the spin imparted to the individual fragments as a function of Q-value are extracted for the three reactions.

E NUCLEAR REACTIONS ^{176}Yb, ^{148}Sm, ^{nat}Ag(^{165}Ho, X), E = 1400 MeV; measured γ-ray multiplicity, anisotropy, continuum γ-rays; deduced fragment spin distributions.

1. Introduction

In deeply inelastic collisions, a certain fraction of the initial orbital angular momentum is converted into spin of the individual fragments [1]. This process has been investigated by studying the decay of the highly excited nuclei emerging from the primary reaction. Measurements of the sequential emission of α-particles [2–4], fission fragments [5–9] and γ-rays [10–22] have provided information on different parameters of the spin distributions, generated as a consequence of the interaction between the two reaction partners. In principle, one can expect that these distri-

† Permanent address: Comisión Nacional de Energía Atómica, Buenos Aires, Argentina.
†† Permanent address: Institute of Atomic Energy, Beijing, China.
††† Permanent address: Department of Chemistry and National Superconducting Cyclotron Lab., Michigan State University, East Lansing, Michigan 48824, USA.

butions will reflect the underlying mechanism responsible for the angular momentum transfer. For example, the average values of the spins imparted to both deep-inelastic fragments can be related to the rotation regime of the dinuclear complex. On the other hand, the spin fluctuations (both in magnitude and orientation) not only reflect the diffusive nature of the angular-momentum-transfer process, but also, they carry information on the rotational degrees of freedom involved. However, if the rotational modes of the dinuclear complex reach a state of statistical equilibrium with the intrinsic degrees of freedom, then the distinction among different possible mechanisms would be very difficult since all of them would lead to essentially the same spin distributions. Therefore, the knowledge of the statistical equilibrium behavior and its comparison to experimental results seems to play an important role in the comprehension of the spin-transfer process.

The limit of statistical equilibrium has been investigated in refs. [23,24]), assuming a very simplified configuration for the intermediate dinuclear complex. In this model, the thermal excitation of the rotational modes of the system gives rise to random generation of the associated angular momentum components. These, in turn, couple to those components arising from rigid rotation, which are aligned perpendicular to the reaction plane, and the net result is a distribution in magnitude and orientation of the angular momenta in the system. For mass-symmetric systems, the model predicts a gaussian distribution for the cartesian components of the spins, with almost equal variances along the three coordinates [23]). The magnitude of the resulting fluctuations were compared to the results from the reaction ^{165}Ho + ^{165}Ho at 8.5 MeV/nucleon, studied via γ-ray multiplicity and anisotropy techniques [22]). It was shown that the relatively small anisotropies observed at small Q-values could be explained by the thermal excitation of the rotational modes of the dinuclear complex. For extreme mass asymmetries, the statistical model predicts that the spin distribution of the heavy fragment will develop a strong in-plane asymmetry, produced by the enhancement of the fluctuations along the line of centers of the complex [24]). This prediction was tested through the measurement of in-plane angular distributions of sequentially emitted fission fragments in the reaction of ^{20}Ne + ^{238}U and ^{197}Au at 12.6 MeV/nucleon [8]). The results showed a large in-plane anisotropy, indicating a strong asymmetry of the spin distribution, but it was also shown that a large uncertainty exists in the determination of the line between centers at the time of scission of the dinuclear complex.

In the present paper we report the results of a systematic investigation of the magnitude and the alignment of the spins imparted to both deep-inelastic fragments in the reactions of 8.5 MeV/nucleon ^{165}Ho on targets of ^{175}Yb, ^{148}Sm and ^{nat}Ag. The systems studied lie in the region of small to moderate mass asymmetries. For this region, the statistical model predicts that for each fragment, the variances of the spin distributions along the three cartesian coordinates are nearly equal, although the fluctuations are significantly larger for the heavier fragment. The experimental technique used in this study was the measurement of the multiplicity

and the anisotropy of unresolved γ-rays. In the mass region covered by the projectile and the targets, a strong correlation between γ-ray multiplicities and spin magnitudes can be expected [15,25]. The extracted average spin magnitudes for each reaction were combined with the predicted variances, to calculate anisotropies that were finally compared with experimental values. The targets and the projectile used in this reaction fall into two categories. The ^{176}Yb and ^{165}Ho isotopes lie in the region of the good rotational nuclei, and therefore, the subsequent electromagnetic cascades are enriched in 'stretched' quadrupole transitions. These γ-rays are predominantly emitted along directions contained in the plane perpendicular to the spin of the emitter, thus the anisotropies of the angular distributions are very sensitive to the degree of alignment. On the other hand, ^{148}Sm and both isotopes in ^{nat}Ag are well removed from this region of good rotors, thus the corresponding γ-ray spectra will have fewer stretched quadrupole transitions. The effect that the uncertainty in the composition of multipolarities has on the determination of the parameters of the spin distributions are discussed.

2. Experimental techniques

A beam of ^{165}Ho at 1400 MeV from the Lawrence Berkeley Laboratory Super-HILAC was used to bombard self-supporting targets of ^{176}Yb, ^{148}Sm, and ^{nat}Ag with thicknesses 0.90 mg/cm^2, 0.46 mg/cm^2, and 0.97 mg/cm^2, respectively. The beam current during the experiment varied between 3 enA and 7 enA. The detection system and its geometrical arrangement was similar to that described in detail in ref. [22]), except for the addition of a multiplicity filter [4]). Therefore, only a brief outline will be given below.

2.1. DETECTION SYSTEM

Three surface-barrier silicon detectors (300 μm thick) were used to detect the projectile-like fragments emerging from the binary deep-inelastic reaction. Two of them (Si-1 and Si-3) were located in a horizontal plane, parallel to the scattering-chamber floor. The third detector (Si-2) was mounted on an arc situated in the vertical plane that contains the beam axis. The three detectors were at a distance of 14.3 cm from the target and were collimated to 1.1 cm in diameter.

The γ-ray detectors consisted of three externally mounted 12.7 cm diameter by 15.2 cm deep NaI scintillators, which looked at the target through identical 0.6 cm thick lucite windows on the scattering chamber. The distance of 60 cm between the target and the detectors provided an adequate separation of neutrons and γ-rays by time of flight. Two of these counters (NaI-1 and NaI-3) were placed in the scattering-chamber plane and the third one (NaI-2) was 90° out of this plane.

In addition to the particle detectors and large NaI counters, an array of eight 7.6

cm × 7.6 cm NaI counters was used as a multiplicity filter. These detectors were located above the scattering chamber in an axially symmetric arrangement with respect to the vertical direction. Each detector was spaced 45° from the next, and they all looked at the target through a 3 mm aluminium dome from an angle of 45° and at a distance of 23 cm. This multiplicity filter was used both to obtain an additional independent measurement of the average multiplicity and to enable the biasing of the spin distribution toward higher values.

The geometry of the whole detection system was such that several redundant measurements of the γ-ray multiplicity and anisotropy could be made. Particle detectors Si-1 and Si-3 on the one hand and Si-2 on the other defined, together with the beam axis, two mutually perpendicular reaction planes. Each NaI detector provided either an in-plane or an out-of-plane measurement, depending on whether it was in coincidence with Si-1, Si-2, or Si-3. The out-of-plane angles θ (measured from the *perpendicular* to the corresponding reaction plane) given by the various Si-NaI combinations are summarized in table 1.

TABLE 1

Angles between each γ-ray detector and the perpendicular to the reaction plane defined by each particle detector

	Si-1	Si-2	Si-3
NaI-1	90°	0°	90°
NaI-2	0°	90°	0°
NaI-3	90°	30°	90°

2.2. CALIBRATIONS AND CORRECTIONS

The energy calibration of the particle detectors was performed using the kinematically calculated energies of the elastic peaks from the different reactions. Additional corrections were made for the energy loss in the target material [26] and for the pulse-height defect [27] in the silicon detectors. The energy calibration of the large NaI crystals was made using the 570 keV and 1064 keV γ-rays from the ^{207}Bi decay. For the efficiency calibrations, one of the coincident transitions from either ^{60}Co, ^{207}Bi, or ^{152}Eu was detected in a Ge(Li) detector while the other was looked for in one of the NaI crystals. The detector efficiency was then calculated as the coincidence-to-singles ratio, corrected for the angular correlation, internal conversion, and branching ratios of the decay. The efficiency calibration of the multiplicity array was done in a similar fashion. In this case, one of the eight detectors of the same array was used as a trigger for the other seven.

Corrections to the γ-ray energies (Doppler shift), angles of emission, and solid

angles (aberration) had to be considered in order to account for the fact that the emission takes place from moving sources. The relevant formulae are [28])

$$E_\gamma(\xi) = \frac{E_\gamma^0(1-\beta^2)^{\frac{1}{2}}}{1-\beta\cos\xi}, \tag{1a}$$

$$\cos\xi = \frac{\cos\xi^0 + \beta}{1+\beta\cos\xi}, \tag{1b}$$

$$\frac{d\Omega^0}{d\Omega} = \frac{1-\beta^2}{(1-\beta\cos\xi)^2}. \tag{1c}$$

In these equations, E_γ is the γ-ray energy, β is the speed of the emitter in units of the speed of light, ξ is the angle between the detector and the velocity of the emitter, and Ω is the solid angle. In all cases, the superscript "0" refers to quantities measured in the reference frame where the emitter is at rest. In spite of the simplicity of these equations, it is not possible to perform an exact correction because there are *two* possible emission sources that cannot be experimentally distinguished. The magnitude of the energy shift (eq. (1a)) was estimated by assuming that all the γ-rays were emitted either from the projectile-like fragment or from the target-like fragment. The resulting spectra were then added together, weighted by the corresponding solid-angle correction (eq. (1c)). These "corrected" spectra were very similar to the uncorrected ones. This is not unexpected since, for most Si-NaI combinations, the sign of $\cos\xi$ changes depending on which fragment is considered to be the emitter, thus given rise to almost an exact cancellation. Finally, it was estimated from eq. (1b) that the angles θ^0, measured in the reference frame where the emitter is at rest, differed from those listed in table 1 by less than 6°, even for the most unfavorable cases.

Due to the incomplete photopeak efficiency of the NaI detectors, the true γ-ray spectral shapes must be obtained by unfolding the raw pulse-height spectra. However, it was shown in a previous work [22]) that, within experimental errors, the unfolding procedure did not affect the values of the multiplicities or anisotropies. Therefore, the results presented in the remainder of this paper have been obtained from the raw spectra.

2.3. DATA ACQUISITION AND ANALYSIS

The signals generated in the various detectors were processed by means of NIM-standard electronic modules. Data were taken in an event-by-event mode and written onto magnetic tape. Each event consisted of 12 parameters: the pulse heights from the three Si detectors and the three NaI counters, the four TAC signals (one for each large NaI and one for the multiplicity array), the N-fold distribution from the multiplicity array and a marker of the scaled-down particle-

singles. The "master gate", used in the definition of an event, was opened by (i) scaled-down heavy-ion singles, (ii) heavy-ion (NaI) coincidences, and (iii) heavy-ion (multiplicity filter) coincidences.

The data analysis proceeded along the following lines. Heavy-ion singles and heavy-ion (multiplicity filter) coincidence data were directly sorted from the raw-data tapes and written in histogram form for further processing. Heavy-ion (NaI) coincidences were stripped from the raw data and rewritten on tape in event-by-event form. Due to the lower probability for such coincidences, this procedure substantially reduced the number of data tapes to be analyzed.

3. Experimental results

The primary quantities of interest extracted from the data are: (i) heavy-ion energy spectra, (ii) γ-ray energy spectra as a function of Q-value, and (iii) distribution of N-fold coincidences in the multiplicity filter, as a function of Q-value.

3.1. PARTICLE-ENERGY SPECTRA

The three heavy-ion detectors were placed at 28°, 25°, and 19° to the beam axis for the ^{176}Yb, ^{148}Sm, and ^{nat}Ag targets, respectively. These angles are slightly behind the classical grazing angle of each reaction. Fig. 1 shows the energy spectra obtained at those angles as well as the particle-energy gates used in the analysis of the γ-ray data. For the three systems the spectra exhibit both an elastic and a deep-inelastic peak.

The calculation of Q-values associated with different detected heavy-ion energies was done assuming that only two fragments (equal to the initial projectile and target) were present in the exit channel. The resulting values were iteratively corrected for the effect of neutron evaporation on the energy of the detected heavy ions, assuming that one neutron was emitted for every 12 MeV of excitation energy.

3.2. GAMMA-RAY DATA FROM THE LARGE NaI DETECTORS

In-plane and out-of-plane continuum γ-ray energy spectra in coincidence with a projectile-like fragment were recorded using the various redundant combinations of particle and γ-ray detectors listed in table 1. Average multiplicities per event for different γ-ray energy intervals were calculated from the number of coincidences, the number of particles singles, and the efficiency of the γ-ray counter. Finally, the anisotropies as a function of Q-value were calculated as the ratios of in-plane to out-of-plane γ-ray multiplicities.

3.2.1. Gamma-ray energy spectra. The shape of the unresolved γ-ray spectra from

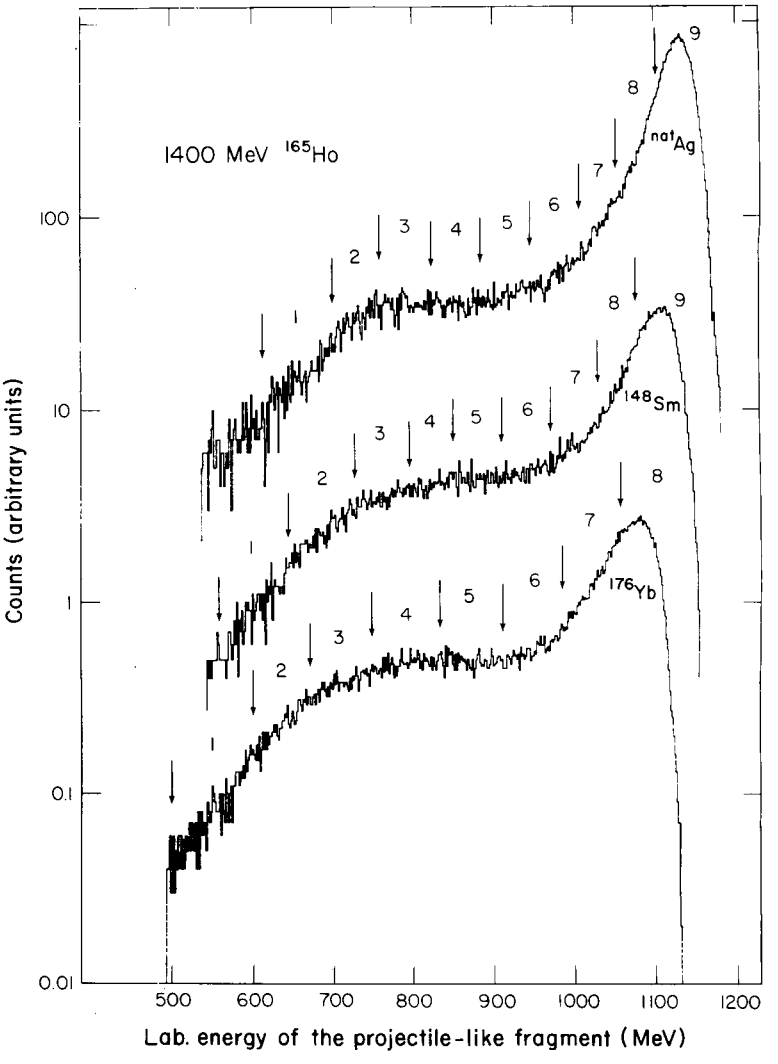

Fig. 1. Representative energy spectra of the projectile-like fragments in the laboratory reference system for three reactions. The target nucleus is indicated in the upper right hand portion of each spectrum. The arrows indicate the boundaries of the gates used for the analysis of the coincidence γ-ray data.

the three reactions have the same qualitative characteristics. A representative example of an in- and out-of-plane spectrum from the reaction ^{176}Yb + ^{165}Ho is shown in fig. 2. An intense bump dominates the low-energy portion of the spectrum, followed by an exponential tail that extends to much higher energies. The bump region exhibits a pronounced in-plane peaking, suggesting that it is predominantly composed of stretched quadrupole γ-rays emitted from nuclei with their spins aligned mostly perpendicular to the reaction plane. The enrichment of

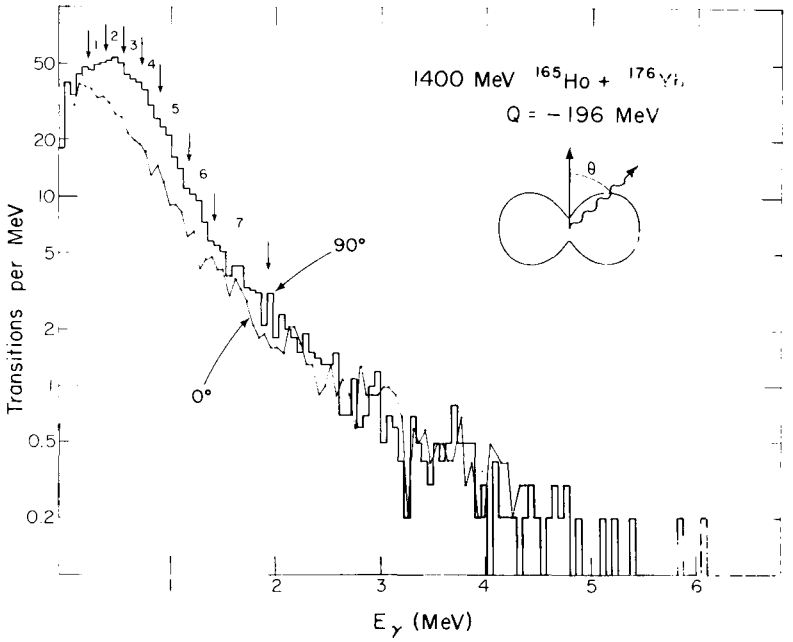

Fig. 2. Comparison between typical unresolved γ-ray spectra recorded at 90° (in-plane) and 0° (out-of-plane) in coincidence with heavy ions for $Q \simeq -196$ MeV. The normalization is such that the areas under the curves are equal to $M_\gamma(90°)$ and $M_\gamma(0°)$, respectively (see eq. (3)). The arrows indicate the boundaries of the gates used to investigate the dependence of various quantities on E_γ (see text).

the low-energy region in stretched E2 γ-rays is a well-known feature of reactions leading to rotational compound nuclei[29]). The higher energy portion of the spectrum ($E_\gamma \geqq 2$ MeV), thought to be a mixture of stretched and unstretched electric dipole transitions[30,31]), shows no appreciable anisotropy.

Fig. 3 shows the dependence of the spectral shape of the continuum γ-rays on the reaction Q-value. The upper-energy edge of the bump moves towards higher γ-ray energies with decreasing Q-value across the quasielectric region, until it saturates in the deep-inelastic region. Since for a rotational nucleus the maximum energy of the stretched E2 γ-rays is related to the spin at the top of the cascade, this behavior of the edge of the bump is an indication of the dependence of the fragments' maximum spins upon Q-value.

3.2.2. Gamma-ray multiplicity. For a given Q-value, the area (N_c) under any portion of each γ-ray spectrum is proportional to the average multiplicity $\langle M_\gamma \rangle$ of the γ-rays in the corresponding γ-ray energy interval. The proportionality constant includes the efficienty (ε) of the NaI detectors, the number of heavy-ion singles (N_s) and the γ-ray angular distribution $W(\theta)$:

$$\langle M_\gamma \rangle = \frac{N_c}{N_s W(\theta) \varepsilon}, \qquad (2)$$

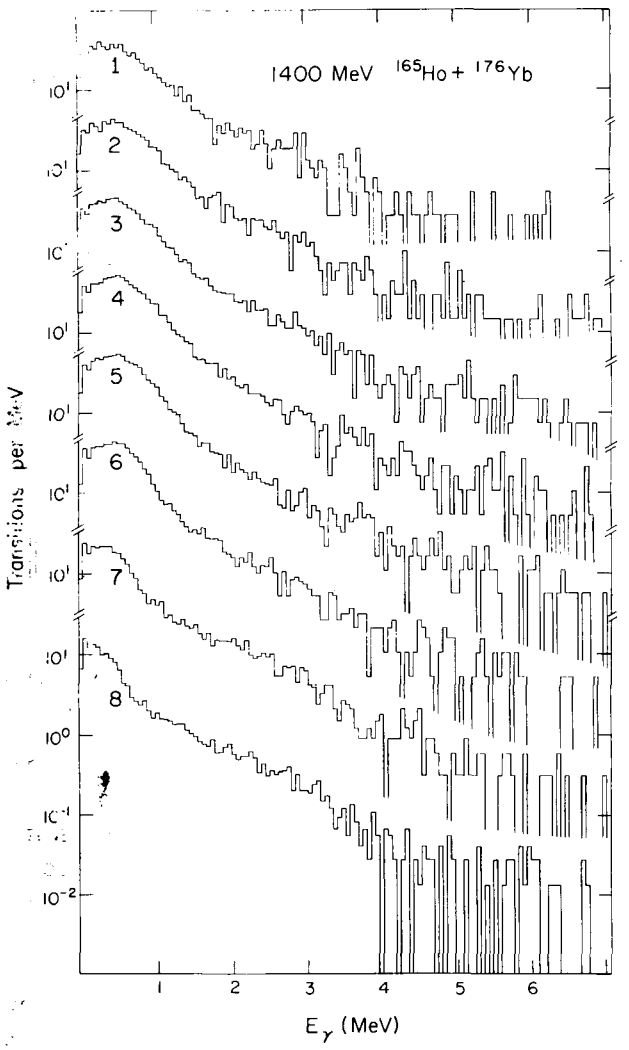

Fig. 3. Typical one-fold γ-ray spectra obtained in coincidence with heavy ions. The numbers 1–8 correspond to the Q-value gates indicated in fig. 1. Note the evolution of the low-energy "bump" when going from elastic or quasielastic (spectrum 8) to the most inelastic (spectrum 1) collisions.

where θ is the angle between the axis of the γ-ray detector and the perpendicular to the reaction plane. We define the in-plane and out-of-plane multiplicities [$M_\gamma(90°)$ and $M_\gamma(0°)$, respectively] as follows

$$M_\gamma(90°) = \langle M_\gamma \rangle W(90°), \qquad M_\gamma(0°) = \langle M_\gamma \rangle W(0°). \tag{3}$$

The redundant geometry was very important in the evaluation of possible system-

atic errors (especially those arising from small changes in the scattering angles due to changes in the beam position, and uncertainties in the evaluation of Doppler-shift and aberration corrections). The values of the experimental multiplicities quoted in the rest of the paper correspond to averages of the various combinations of Si and NaI detectors. The error bars shown include contributions from the variance associated with the spread of the combinations about the average as well as the typical statistical errors of an individual measurement.

Fig. 4 shows $M_\gamma(90°)$ (squares) and $M_\gamma(0°)$ (triangles) for γ-rays with energy above 300 keV as a function of Q-value. The general trend of these data is similar for the three systems and agrees with that previously observed in the ^{165}Ho + ^{165}Ho reaction [22]). There is a rapid rise across the elastic and quasielastic (QE) region, followed by a saturation or even a slight decrease for the most deep-inelastic (DI) events. Whereas $M_\gamma(90°)$ (in-plane) actually peaks and then decreases slightly, $M_\gamma(0°)$ (out-of-plane) exhibits a plateau (^{148}Sm and ^{nat}Ag data) or even a slow monotonic increase (^{176}Yb). As indicated by eq. (3), the different behavior of $M_\gamma(0°)$ and $M_\gamma(90°)$ reflects the angular distribution of the radiation. The maximum value of the γ-ray multiplicity decreases with the mass of the target (40, 37,

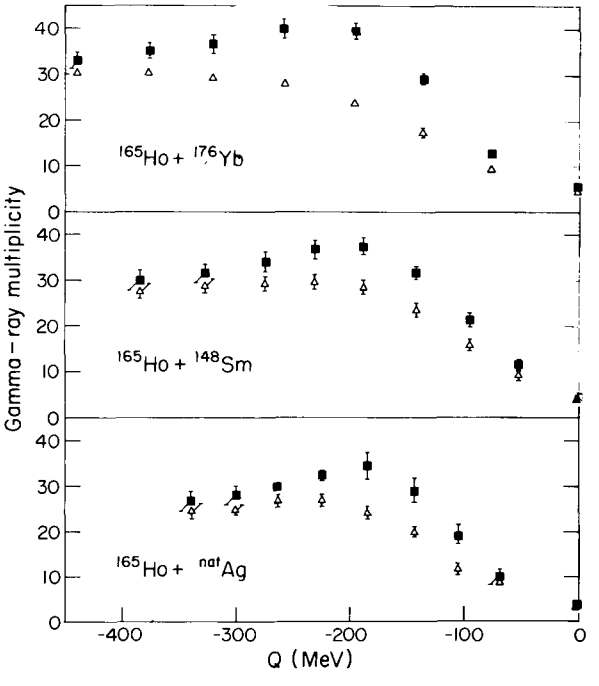

Fig. 4. "In-plane" (squares) and "out-of-plane" (triangles) multiplicities as a function of Q-value for the ^{165}Ho + ^{176}Yb, ^{148}Sm and ^{nat}Ag reactions for heavy ions detected at 28°, 25° and 19°, respectively. According to the definition of these quantities (eq. (3)), the difference between the two curves for each reaction reflects the angular distribution of the radiation.

and 33 for ^{176}Yb, ^{148}Sm, and ^{nat}Ag, respectively). In the next sections we shall discuss in more detail the connection between the experimental multiplicities and both the fragments' spins and the multipolarity mixing ratios as a function of γ-ray energy.

3.2.3. Gamma-ray anisotropy. We define the anisotropy as the ratio of the in-plane to out-of-plane multiplicities:

$$\mathscr{A} = M_\gamma(90°)/M_\gamma(0°). \tag{4}$$

This quantity depends on the alignment of the spin distribution and the multipolarity mixing ratios of the radiation. For pure stretched quadrupole γ-rays emitted from a perfectly aligned ensemble of nuclei, an infinite anisotropy would be predicted [32]). Even if there is a moderate admixture of isotropic transitions (~ 30 %), the γ-ray angular distribution would still exhibit a deep minimum along the alignment direction and thus the anisotropy should still be quite sensitive to fluctuations in the spin orientation.

Fig. 5 shows the γ-ray anisotropy as a function of Q-value for the three different

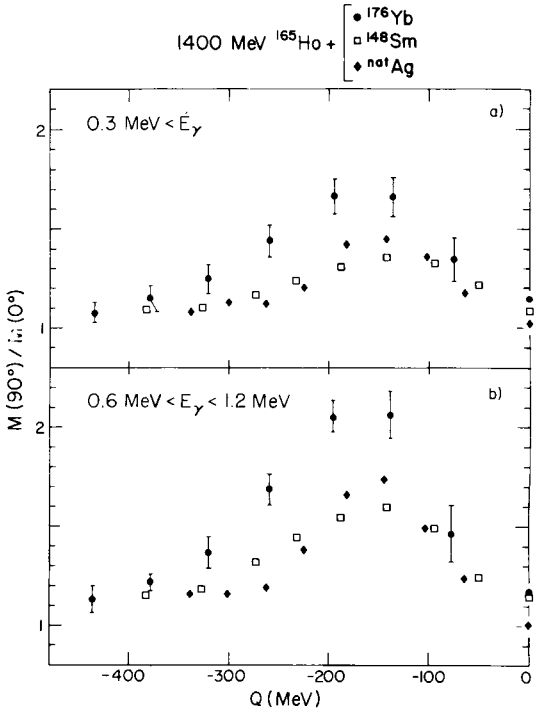

Fig. 5. Gamma-ray anisotropy as a function of Q-value, for heavy ions detected near the grazing angle. In part (a), γ-rays of all energies above 0.3 MeV are considered. Part (b) shows that by restricting the γ-ray energies, the anisotropy increases for all three reactions. Error bars for the three systems' points are similar and are only shown for the ^{165}Ho + ^{176}Yb system.

reactions and for two different γ-ray energy intervals. In all cases the anisotropy increases throughout the QE region and then falls across the DI region. The peak value for the $^{176}Yb+^{165}Ho$ reaction is much higher than for the other two reactions. As anticipated, the selection of the γ-ray energy interval in the bump region produces a significant increase of the anisotropy (fig. 5b) as a consequence of the enrichment in stretched E2 transitions in this energy region.

The Q-value dependence of the anisotropy can be qualitatively understood in terms of the evolution of the degree of spin alignment. For very low negative Q-values, the interaction time is short compared to the relaxation times of the rotational degrees of freedom of the system, and therefore little angular momentum is converted into spin. Even small fluctuations can destroy the spin alignment, thus the angular distribution is almost isotropic. More inelastic collisions tend to dissipate an increasing fraction of the initial angular momentum (as indicated by the multiplicity curves), while the fluctuations remain at a relatively low level. This causes the anisotropy to rise rapidly. Finally, for the most inelastic events the amount of angular momentum transferred to intrinsic rotation saturates while the spin fluctuations (caused by both the statistical excitation of spin depolarizing modes and by neutron evaporation) continue to increase. This indicates that the constant spin observed as the Q-value decreases is made up of a progressively larger contribution from randomly oriented components, and therefore the anisotropy falls.

The dependence of the anisotropy on γ-ray energy for a fixed Q-value (fig. 6) reflects mainly variations in the multipolarity mixing ratios. These curves show a

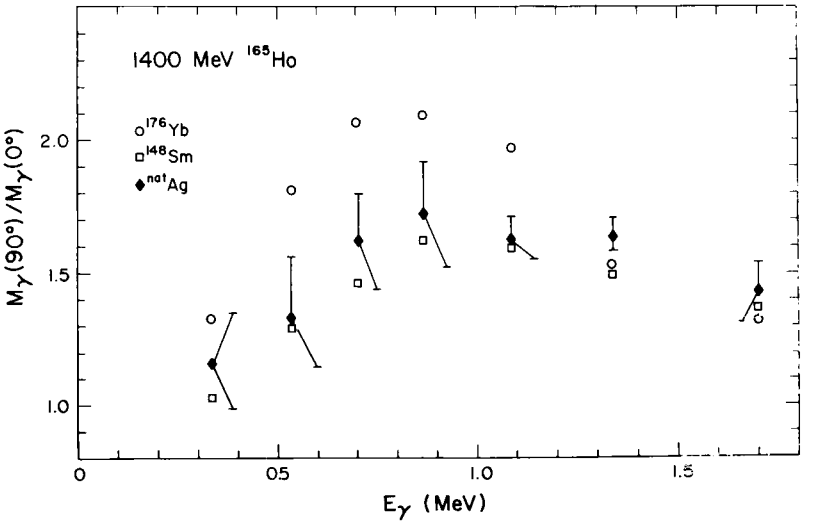

Fig. 6. Gamma-ray anisotropy as a function of γ-ray energy. The Q-value region is constant for each reaction and corresponds to the maximum observed anisotropies. These E_γ intervals correspond to the gates indicated in fig. 2. The anisotropy of the γ-rays with $E_\gamma > 2$ MeV varies between 1 and 1.1 in all cases (not shown in this figure).

large increase through the low-energy region reaching a maximum at $E_\gamma \simeq 0.9$ MeV, followed by a gentle fall to unity for larger values of E_γ. The behavior of the high-energy portion ($E_\gamma \gtrsim 0.9$ MeV) may be understood in terms of a decreasing percentage of stretched quadrupoles (dominant in the upper part of the bump region) and an increasing percentage of isotropic transitions (dominant above 2 MeV). The relatively small anisotropies observed at $E_\gamma \simeq 0.5$ MeV likewise indicate a small percentage of stretched E2 transitions in this energy region. An alternative possibility is that these low-energy γ-rays are emitted from states where an additional depolarization occurred due to hyperfine interactions [33]).

3.3 MULTIPLICITY-FILTER DATA

The analysis of the distribution of the number of γ-rays detected in the 7.6 cm × 7.6 cm NaI detectors in coincidence with a heavy ion provided an independent measurement of the average γ-ray multiplicity as a function of Q-value. The formalism used was that of Sarantites *et al.* [34]). For the three reactions the multiplicities obtained using the multiplicity filter were in very good agreement with those extracted from the individual large NaI detectors.

Data from the multiplicity filter can also be used to study the dependence of the anisotropy on the spin magnitude. By requiring high-order coincidences in the multiplicity filter one should select, on average, events associated with a larger number of γ-rays and therefore higher spins. To investigate this effect, we have applied the following procedure. First, we considered all the events that included coincidences among a particle detector, a large NaI detector, and the multiplicity filter. Additional requirements were that the energy of the heavy ions fell into one of the Q-value bins indicated in fig. 1, and that at least two detectors of the multiplicity filter fired. We define N_T as the number of these "triple" coincidences (Si-NaI array). Next, we removed the condition on the large NaI detectors and considered events that satisfied only the other requirements listed above. The total number of these "double" coincidences (Si array) was defined as N_D. In analogy with eqs. (2) and (3), we define

$$m_\gamma(\theta) = \frac{N_T}{N_D \varepsilon} . \tag{5}$$

This ratio may be interpreted as approximately equal to the average number of γ-rays associated with the "biased" population, after excluding the two or more γ-rays detected in the multiplicity filter. Fig. 7a compares $M_\gamma(90°)$ and $m_\gamma(90°)$ as a function of Q-value. The open squares, corresponding to the biased spin population, are systematically higher by about three γ-rays (fig. 7a), even without considering those already detected in the multiplicity filter. The relative difference seems to be even larger for the three highest Q-value bins.

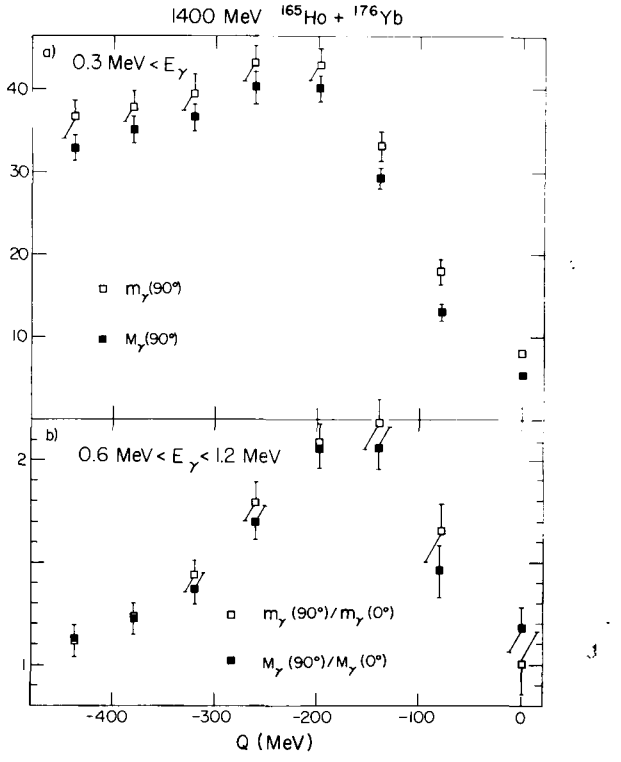

Fig. 7. (a) Average γ-ray "multiplicities" with (open squares) and without (filled squares) the requirement on the multiplicity filter (see text for discussion). (b) Gamma-ray "anisotropies" with and without requirements on the multiplicity filter (see text for discussion).

Fig. 7b shows a comparison between the quantities $M_\gamma(90°)/M_\gamma(0°)$ (filled squares) and $m_\gamma(90°)/m_\gamma(0°)$ (open squares). Both sets of data points are in agreement within error bars, although the γ-rays emitted from the biased population exhibit a somewhat larger "anisotropy". A more quantitative interpretation of this data in connection with the alignment of the biased population is hindered by the complex angular-correlation effects associated with the detection of two or more γ-rays at an angle of 45° from the reaction plane.

4. Theory and model calculations

In this section we shall present the theoretical aspects involved in the extraction of information about the spin-transfer process from the experimental results. Some of the subjects which are only briefly considered here have been extensively discussed elsewhere [1]).

4.1. ANGULAR MOMENTUM TRANSFER AND STATISTICAL EQUILIBRIUM

During a deep-inelastic collision the reaction partners form a short-lived dinuclear system [35,36]. The portion of the interaction responsible for the conversion of orbital angular momentum into intrinsic spin can be viewed as a dissipative process in which frictional forces oppose the mutual sliding or rolling of the nuclear surfaces in contact. Several models have been postulated to explain these effects in terms of specific mechanisms, such as particle transfer [37,38] or the excitation of surface modes [39]. A common feature of all these descriptions is that they predict a distribution of transferred spins, rather than a well-defined value. The characteristics of the spin distribution are dictated essentially by (i) the choice of a particular set of angular-momentum-bearing degrees of freedom, and (ii) the equilibration time (associated with the transfer mechanism) relative to the lifetime of the complex.

The observation of a rigid-rotation regime of the dinuclear system in many reactions [2,4,11,15] points to the statistical relaxation of the rotational modes and suggests the feasibility of an equilibrium statistical approach to the study of the angular momentum transfer. Regardless of whether complete equilibration is actually attained during the collision, the study of the long-time limit is interesting in its own right because it does not depend on the particular transfer mechanism. Therefore, if one describes the intermediate complex by means of an adequate set of degrees of freedom, the equilibrium limit will provide a natural reference for comparison with experimental results. Furthermore, the applicability of equilibrium statistical results does not necessarily require that the system reach equilibrium. Indeed, we shall see that the model has been used only to calculate the variances of the distribution, which may approach their equilibrium values faster than the average spins [40].

The equilibrium limit of the angular momentum partition in deep-inelastic reactions has been investigated in refs. [23,24]. In this model, the dinuclear system is represented by two touching rigid (but not rigidly attached) spheres, whose normal modes can be thermally excited through their coupling to the internal degrees of freedom. The associated random components of the angular momentum, when added to the aligned component arising from rigid rotation, give rise to a distribution in both the magnitude and orientation of the fragments' spins. Under these assumptions, the widths of the distribution along the three cartesian coordinates may be expressed as a function of the temperature, the mass asymmetry, and the total mass of the system.

Let us now turn to the interpretation of the data in terms of this equilibrium model.

4.2. MODEL CALCULATIONS

The ultimate goal of our investigation is to obtain information on the fragments'

spin distributions, i.e. average spin magnitudes, average aligned component, and degree of alignment (P_{zz}). Unlike the mass-symmetric ^{165}Ho + ^{165}Ho case [22]), in the present study one must allow for different spin distributions associated with each fragment. Since the spin distributions are not directly measured, the model calculations must be used to predict observed quantities such as the γ ray anisotropies. The agreement (or lack thereof) between the calculations and the data serves as a measure of the confidence that we can place in the inferred parameters of the distribution. All these parameters depend on one another, and therefore almost the totality of the extracted information is model dependent to some extent. However, we shall see that in many cases the dependence of the theoretical results on different assumptions is surprisingly weak.

4.2.1. Spin distribution. The calculation of the spin distributions combines results from both the experiment and the equilibrium statistical model. The first extracted quantity from the experiment is the average value of the sum of spin magnitudes. Based on compound-nucleus work we have assumed that in the most general case the admixture of multipolarities in the γ-ray cascade includes stretched quadrupole, stretched dipole, and statistical transitions that remove 2, 1, and 0 $\hbar$ of fragment spin, respectively. If the number of each type of γ-ray per reaction with energies above the experimental threshold, is N_2, N_1, and N_{is}, then the observed multiplicity M_γ is

$$M_\gamma = N_2 + N_1 + N_{is}. \tag{6}$$

For the compound nucleus case, the average spin at the beginning of the γ-ray cascade is given by

$$\langle I \rangle = (2N_2 + N_1) + \Delta, \tag{7}$$

where Δ is the spin removed by transitions with energies below the 0.3 MeV threshold [22]). To apply eq. (7) to a binary reaction, all the quantities involved should correspond to the fragment whose spin is being calculated. Unfortunately only the total multiplicity of the γ-rays emitted by *both* fragments is known. At this point we have assumed that the total number of stretched transitions is partitioned between the two fragments according to the ratio of their moments of inertia as would be given by rigid rotation. This assumption is consistent with the equilibrium approach, thus its validity may be questionable for the highest Q-values.

According to the statistical model, the spin distribution for each fragment is

$$P(I_x, I_y, I_z) = \mathcal{N} \exp\left[-\left(\frac{I_x^2}{2\sigma_x^2} + \frac{I_y^2}{2\sigma_y^2} + \frac{(I_z - \langle I_z \rangle)^2}{2\sigma_z^2} \right) \right], \tag{8}$$

where $\mathcal{N}$ is a spin-independent normalization constant. The cartesian reference

system is chosen such that the y-axis coincides with the line between centers, which is also the symmetry axis. For the heavy fragment, the variances σ_x, σ_y, and σ_z are given by

$$\sigma_x^2 = \sigma_z^2 = \frac{\mathcal{I}_H(\mathcal{I}_L + \mu d^2)}{\mathcal{I}_H + \mathcal{I}_L + \mu d^2}\, T, \qquad \sigma_y^2 = \frac{\mathcal{I}_H(\mathcal{I}_H + \mu d^2)}{\mu d^2}\, T. \tag{9}$$

In these equations, the subscripts H and L denote the heavy and light fragment, respectively. $\mathcal{I}$ is the moment of inertia of a (spherical) fragment, μ is the reduced mass of the system, d is the distance between centers, and T is the temperature associated with the intrinsic excitation energy. The variances of the spin distribution for the light fragment are obtained from eq. (9) by simply interchanging the subscripts H and L. The temperature was obtained from

$$T = (-Q/a)^{\frac{1}{2}}, \tag{10}$$

where a is the level density parameter taken to be $\frac{1}{8}A_{\text{total}}$, and A_{total} is the mass number of the composite system.

The effects of neutron evaporation were taken into account using the model of ref. [31]), assuming that one neutron is emitted for every 12 MeV of excitation energy per fragment. This model was used to calculate the average spin magnitude and the variances of the spin distributions at the beginning and at the end of the neutron cascade, respectively. The excitation energies were calculated under the assumption that both fragments had equal temperatures.

The value of the average aligned component for each fragment $\langle I_{1z}\rangle$, $\langle I_{2z}\rangle$ was obtained by solving two equations of the form

$$\langle I\rangle = \mathcal{N}\int I \exp\left[-\left(\frac{I_x^2}{2\sigma_x^2} + \frac{I_y^2}{2\sigma_y^2} + \frac{(I_z - \langle I_z\rangle)^2}{2\sigma_z^2}\right)\right] \mathrm{d}I_x \mathrm{d}I_y \mathrm{d}I_z, \tag{11}$$

where $\langle I\rangle$ is the measured spin magnitude and $\langle I_z\rangle$ is the only unknown.

4.2.2. Angular distributions and anisotropies. The basic angular distributions of stretched quadrupole ($\mathcal{W}_2$) and stretched dipole ($\mathcal{W}_1$) γ-rays emitted from a perfectly aligned system are [32])

$$\mathcal{W}_2(\alpha) = \tfrac{5}{4}(1 - \cos^4\alpha), \tag{12a}$$

$$\mathcal{W}_1(\alpha) = \tfrac{3}{4}(1 + \cos^2\alpha), \tag{12b}$$

where α is the angle between the spin vector and the direction of observation. If the system is misaligned these distributions must be folded into the spin probability distribution function, weighted by the number of transitions of each type (n_{is}, n_1,

and n_2) in a given E_γ region:

$$W(\theta, \phi) \propto \int (n_2 \mathcal{W}(\alpha) + n_1 \mathcal{W}_1(\alpha) + n_{\rm is}) P(I, \theta', \phi') I^2 \mathrm{d}I \mathrm{d}\Omega', \tag{13}$$

where $P(I, \theta', \phi')$ is the spin probability distribution function of eq. (8) expressed in spherical coordinates, and the angle α depends on both the direction of emission (θ, ϕ) and the direction of the spin vector (θ', ϕ') of the emitter:

$$\cos\alpha = \cos\theta\cos\theta' + \sin\theta\sin\phi\sin\theta'\sin\phi' + \sin\theta\cos\phi\sin\theta'\cos\phi'. \tag{14}$$

By writing the angular distribution as in eq. (13), we implicitly assume that all the γ-rays of a given multipolarity have the same angular distribution. If we were to consider the most general case, the coefficients n_1 and n_2 could be functions of I. However, in order to get an analytical result we have neglected this dependence and we have assumed that these coefficients are constants, equal to the average values. The average values of $n_{\rm is}$, n_1, and n_2 were evaluated from the γ-ray energy spectra, as will be discussed in the next subsection. For nearly symmetric systems, the statistical model predicts that the variances σ_x, σ_y, and σ_z are similar to each other. Under the approximation that they are exactly equal to each other, the integral in eq. (13) may be analytically evaluated[42]), and the resulting angular distribution does not depend on the angle ϕ. The common values for the three cartesian variances were obtained from

$$\sigma^2 = \tfrac{1}{3}(\sigma_x^2 + \sigma_y^2 + \sigma_z^2). \tag{15}$$

Two of these average variances were calculated, i.e., one for each individual fragment.

4.2.3. Multipolarity mixing ratios. A significant uncertainty in the input parameters to our model calculation is the multipolarity composition of the continuum γ-ray energy spectra. In an attempt to reduce this uncertainty, we have resorted to results from both compound-nucleus work and the present work.

Rotational nuclei at high spins are known to decay via the emission of basically two types of γ-rays, (i) stretched electric quadrupole transitions, and (ii) "statistical" transitions[25,43]) of nearly isotropic distribution. The energy of the stretched E2 γ-rays are strongly correlated to the spin of the state from which the γ-ray is emitted, and they appear mainly as a low-energy bump in the E_γ spectrum. The statistical transitions (probably an admixture of stretched and nonstretched electric dipoles) are considered to be distributed in energy according to the following function[44]):

$$N_{\rm is}(E_\gamma) \propto E_\gamma^p \mathrm{e}^{-E_\gamma/T}. \tag{16}$$

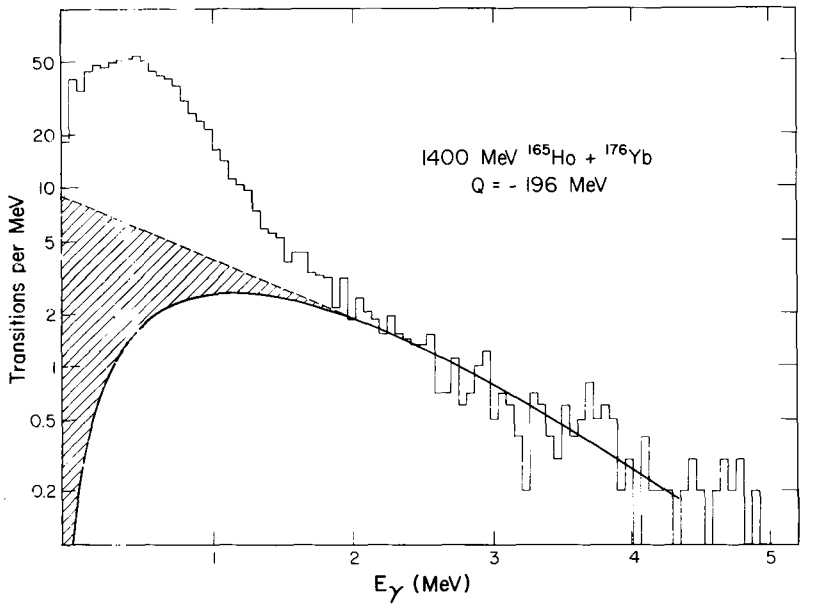

Fig. 8. Decomposition of a typical γ-ray spectrum. The solid line is a fit to the upper portion of the spectrum with the function $KE_\gamma^p e^{-E_\gamma/T}$, where $p = 2$, $T = 0.6$ MeV, and K was adjusted to reproduce the area under the spectrum above 2.25 MeV. The dashed line is an exponential extrapolation to low energies of the high-energy "statistical" tail (see text for discussion).

The solid line in fig. 8 shows a fit of this function (with $p = 2$ and $T = 0.6$ MeV) to the high-energy tail of a typical spectrum. Similar fits were obtained with $p = 3$ and $T = 0.4$ MeV. This decomposition of the spectra indicates that the number of non-statistical γ-rays in a certain energy region (given by the area under the histogram minus the area under the solid curve) increases with decreasing energy. If these transitions were all stretched quadrupoles, the γ-ray anisotropy for a fixed Q-value should decrease monotonically with increasing transition energy across the bump region. Clearly, this prediction is at variance with the low-energy data ($E_\gamma \lesssim 0.9$ MeV) shown in fig. 6. The experimental anisotropies are small for the lowest γ-ray energies, increase and peak at $E_\gamma \simeq 0.9$ MeV, and then fall to unity. This general behavior as a function of E_γ reflects primarily the change of the multipolarity mixing ratios. Indeed, since the Q-value is fixed, the spin depolarization (caused either by particle evaporation or by the reaction itself) is not expected to produce any E_γ dependent effect on the anisotropy.

The decrease of the anisotropy at low E_γ has been observed in previous compound-nucleus works and has been interpreted as evidence for an additional component, likely stretched magnetic dipole transitions[45]). Although the information on the spectral shape of this component is incomplete, it is known that for rotational nuclei these γ-rays are concentrated mainly below 0.5 MeV. For nuclei

in the vicinity of a closed shell, their contribution to the total multiplicity increases significantly [25,43]), and they extend to somewhat higher energies.

To minimize the uncertainties due to this low-energy component in the comparison between the experimental and calculated anisotropies, we have excluded from the analysis all the γ-rays with energies below 0.8 MeV. However, even these low-energy γ-rays must be used in the determination of the sum of the spin magnitudes, so that in principle, the uncertainties in their multipolarities could still affect the determination of important parameters of the spin distributions. In order to estimate the magnitude of this effect, we have considered two extreme situations for the spectral shape of the γ-rays which do not remove angular momentum from the system. First, we assumed that the spectral shape of the statistical transitions ($\Delta I = 0$) is given by eq. (16) (solid curve in fig. 8) and that the rest of the γ-rays are stretched quadrupoles. Under this assumption, the number of stretched quadrupole transitions is overestimated and therefore eq. (7) should provide an upper limit for the total spin. For the low-spin limit, we have assumed that the spectral shape of $\Delta I = 0$ γ-rays is given by the extrapolation to low energies of the high-energy "statistical" tail (fig. 8, dashed line). It may be questioned whether this assumption really represents a low-spin limit for nonrotational nuclei, where the relative contribution of stretched quadrupoles is believed to be small. However, we note that for the three reaction systems, at least one of the two fragments (the projectile-like fragment) has good rotational properties and therefore the number of stretched quadrupole transitions is always significant. This is also confirmed by the fact that even for the ^{nat}Ag and ^{148}Sm targets, the experimental anisotropies reach values of ~ 1.6 (see figs. 5 and 6).

Fig. 9 shows for the ^{165}Ho + ^{148}Sm system that the values of the sum of the spins extracted under the two extreme conditions described above differ by less than 15 %. This result lends justification to the procedure of considering only a restricted portion of the γ-ray spectrum (in which, according to fig. 8, the contribution of the stretched dipole component will be small) for comparison of the model calculation to the anisotropy data. In all the calculations shown in the rest of this paper, we have considered an intermediate situtation by assuming that the γ-rays between the two calculated curves in fig. 8 are stretched dipoles and therefore remove one unit of angular momentum each.

4.2.4. Comparison between the model calculation and the data. Fig. 10 compares the Q-value dependence of the experimental anisotropy to the theoretical calculation, for the region 0.80 MeV $< E_\gamma <$ 0.95 MeV. For all three reactions good agreement is obtained for the most inelastic regions. The shift in the calculated peak anisotropy relative to the data may indicate a breakdown of the statistical equilibrium assumptions. According to the model, the maximum value of the anisotropy should occur when the multiplicity reaches its saturation value.

It must be emphasized that regardless of any assumption made concerning the multipolarity mixing ratios, the most important role in determining the value of

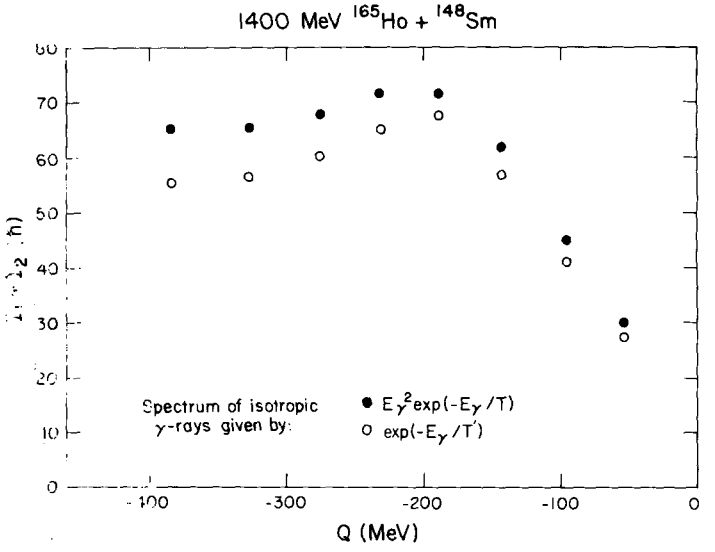

Fig. 9. Sensitivity of the extracted sum of the spins (I_1+I_2) upon the multipolarities of the γ-rays (see text for discussion).

he γ-ray anisotropy is played by the thermal fluctuations. As an illustration, fig. 11 compares the data (open circles) to a calculation assuming no thermal fluctuations dark circles). It is clear that if misalignment is not included, the observed values of he anisotropy cannot be explained.

5 Angular momentum transfer: spin magnitude and alignment

In the last section we have shown that, under the assumption of statistical quilibrium, the model can reproduce the Q-value dependence of the γ-ray anisotropies. In what follows, we shall discuss the behavior of the parameters of the spin stributions (either extracted or calculated, as described in subsect. 4.2.1) that were ed in these calculations of the anisotropy.

. SUM OF SPIN MAGNITUDES AND RIGID ROTATION

Of all the studied quantities, the spin magnitude is the least dependent on model sumptions, since it is closely related to the measured γ-ray multiplicity. However, defining the partition of the total internal angular momentum between the two gments, we have implicitly assumed that the intermediate dinuclear complex aches a state of rigid rotation. In order to test the validity of this assumption, let first analyze the sum of the spin magnitudes I_1+I_2. This quantity is expected to fairly insensitive to any assumption on the rotation regime.

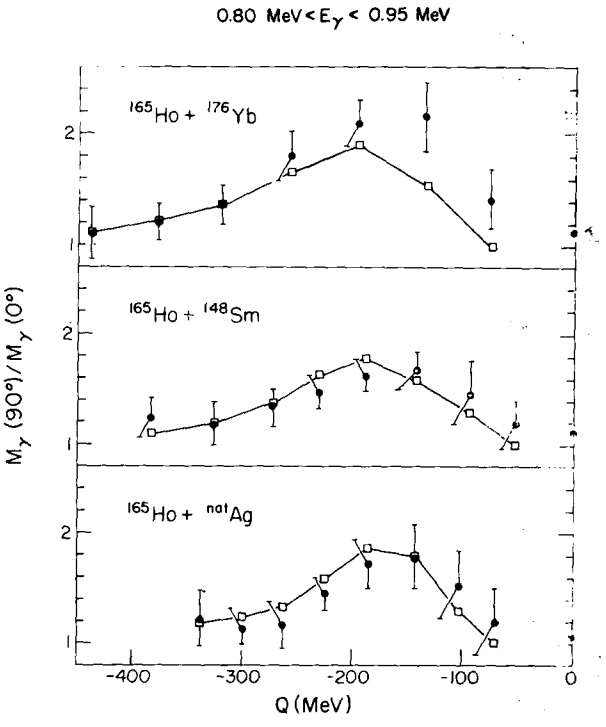

Fig. 10. Comparison between the experimental anisotropies of γ-rays with energies in the interval 0.80 MeV $< E_\gamma <$ 0.95 MeV (circles) and a calculation based on the equilibrium statistical model (open squares) as a function of Q-value. The calculations require some experimental input; therefore they were done only where experimental results were available. The lines are drawn through the calculated points to guide the eye.

Fig. 12 shows $I_1 + I_2$ as a function of Q-value for the three reactions. Two observations can be made. First, the maximum amount of spin corresponding to the saturation region increases with the total mass of the system. Second, the Q-value where saturation is reached appears to become somewhat more negative for heavier systems. To a large extent, this behavior may be attributed to differences in basic parameters of the reaction, such as the Coulomb barrier, total kinetic energy, mass, or angular momentum. A more significant comparison between the reactions can be made by appropriately transforming both axes in fig. 12 so as to remove any factor that is not directly connected to the transfer process itself. The choice of new variables is certainly not unique. For the variable related to the excitation energy we have chosen a transformation from Q-value to temperature (eq. (10)). For the angular momentum axis we have considered two different scales given by the following equations:

$$i_{RR} = \left(\frac{\mathscr{I}_{\parallel}}{\mathscr{I}_{\perp}} I_{max}\right)^{-1} (I_1 + I_2), \tag{17a}$$

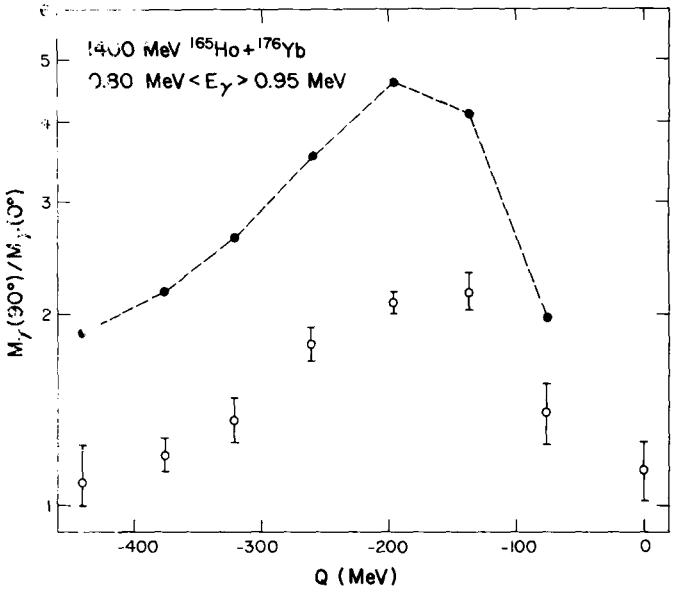

Fig. 11. Comparison between the experimental anisotropies and a calculation that does not include the effect of the thermal fluctuations. The shape of the calculated anisotropies results from both the dependence of the number of emitted neutrons and the composition of the γ-rays (these were the same as those used in the calculated curves of fig. 10) with Q-value.

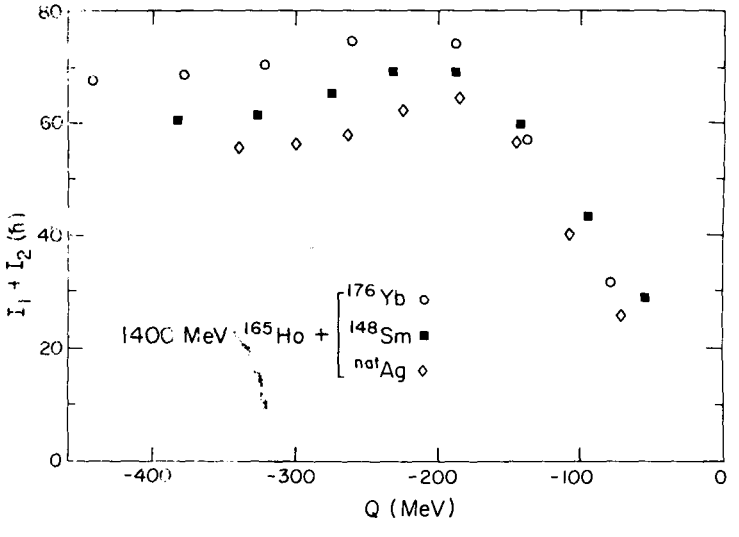

Fig. 12. Sum of the spin magnitudes (I_1+I_2) as a function of Q-value for the three reaction systems.

$$i_{\text{roll}} = (\tfrac{2}{7} I_{\max})^{-1}(I_1 + I_2), \tag{17b}$$

where

$$\mathcal{I}_{\parallel} = \mathcal{I}_1 + \mathcal{I}_2, \qquad \mathcal{I}_{\perp} = \mathcal{I}_{\parallel} + \mu d^2, \tag{18}$$

and $l_{\max}$ is the maximum incoming angular momentum corresponding to a grazing collision. The transformed variables i_{RR} and i_{roll} measure the observed sum of the fragments' spins in units of the maximum value expected from the rigid-rotation and rolling limits, respectively.

Fig. 13 shows plots of the experimental values of i_{RR} and i_{roll} as a function of T. A

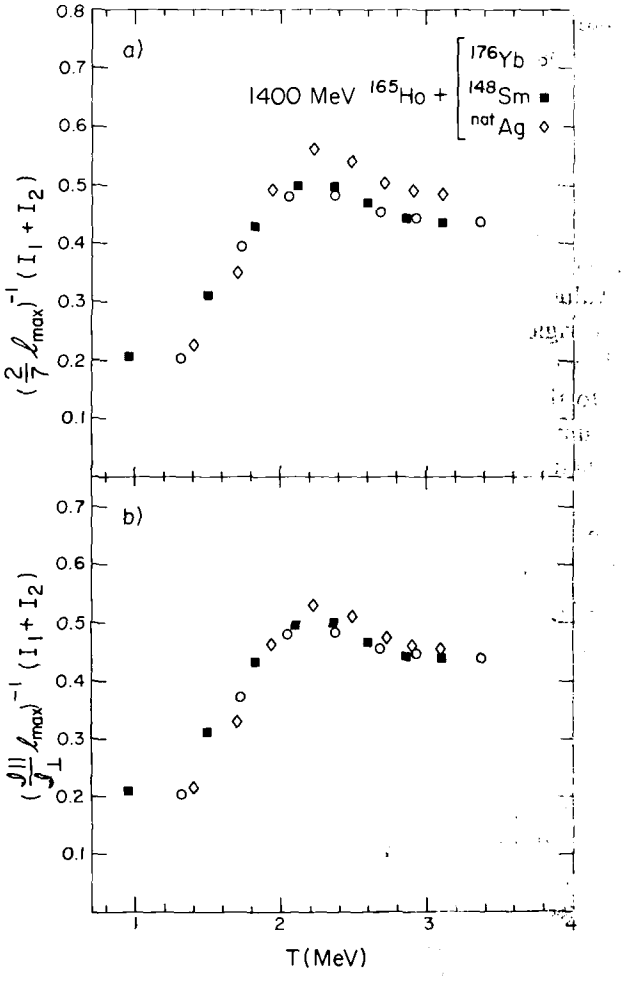

Fig. 13. The sum of spins in reduced units as a function of temperature. The angular momentum axes have been scaled according to the "rolling" limit for part (a) and to rigid-rotation limit for part (b).

comparison between figs. 12 and 13b indicates that the transformation from I_1+I_2 and Q to i_{RR} and T succeeds in reducing the experimental points to essentially a single curve. The transformation according to the rolling limit (fig. 13a) gives a similar curve for the nearly symmetric Ho+Sm and Ho+Yb systems but shows a significant deviation for the more asymmetric Ho+Ag. These results provide, if not proof, at least a strong support to the assumption of rigid rotation of the intermediate complex.

5.2. SPIN DISTRIBUTIONS OF THE INDIVIDUAL DEEP-INELASTIC FRAGMENTS

We shall now examine some results concerning the spin distribution of each of the two exit-channel fragments. As described in subsect. 4.2.1, the average spin magnitudes $\langle I_1 \rangle$ and $\langle I_2 \rangle$ were assigned to each nucleus according to the rigid-rotation prescription, and the variances σ_1^2 and σ_2^2 were calculated with the aid of the statistical model (eqs. (9) and (15)) and the experimental temperatures (eq. (10)). Both types of information were finally combined to obtain the individual spin alignments through the quantities $\langle I_{1z} \rangle$ and $\langle I_{2z} \rangle$ (eq. (11)).

Fig. 14 shows the evolution of the average spin magnitude $\langle I \rangle$ (solid curve) and its average aligned component $\langle I_z \rangle$ (dashed curve) for both reaction partners as a function of Q-value. In all cases the heaviest fragment bears the largest spin according to the rigid-rotation partition. The spin of the projectile-like fragment increases slightly with decreasing total mass because the increase of its moment of inertia (relative to the target-like fragment) prevails over the reduction of the total angular momentum. The Q-value dependence is qualitatively the same as that of the γ-ray multiplicities. Following the rise throughout the elastic and quasielastic region, there is a saturation at large negative Q-values. However, at these large negative Q-values $\langle I_z \rangle$ shows a decreasing trend, which leads to a progressive divergence from $\langle I \rangle$. The magnitude of this effect is a function of the mass of the fragment, and it is related to the alignment of the corresponding spin distribution. The degree of spin alignment is usually measured in terms of the quantity P_{zz} defined as

$$P_{zz} = \frac{3}{2}\frac{\langle I_z^2 \rangle}{\langle I^2 \rangle} - \frac{1}{2} = \frac{1}{1+3\sigma^2/\langle I_z \rangle^2} . \tag{19}$$

With this definition, P_{zz} varies from 0 to 1, those extremes corresponding to a completely unaligned and to a perfectly aligned system, respectively.

Fig. 15 shows the value of P_{zz} as a function of Q-value for each individual fragment in the three reactions. The same qualitative behavior can be observed in all cases: the alignment increases rapidly with decreasing Q-value throughout the quasielastic region, followed by a more or less slow decrease (depending on the mass of the fragment) across the deep-inelastic region. For each system, the heavy reaction partner shows a higher degree of alignment.

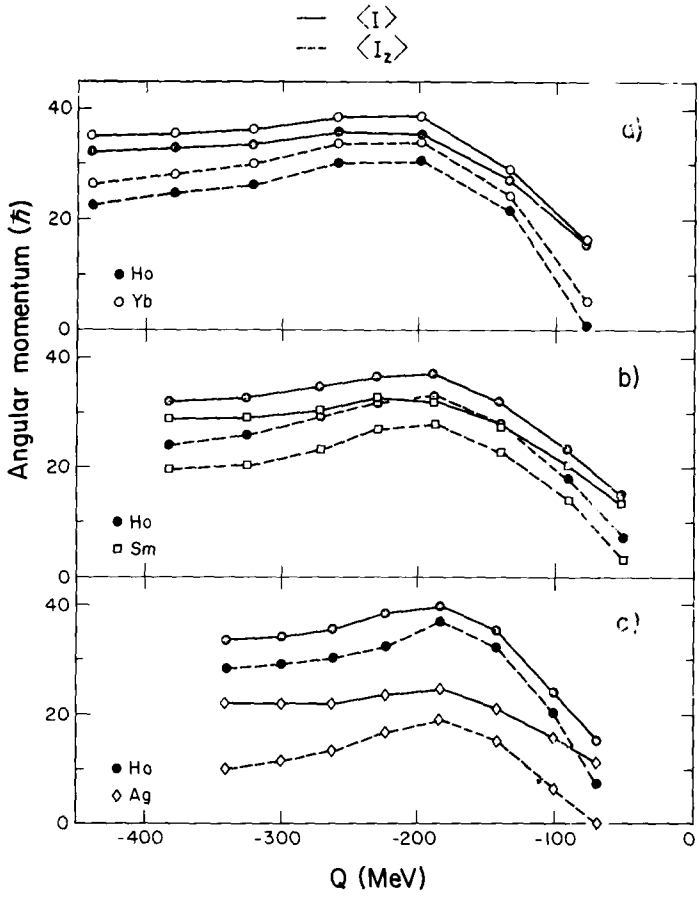

Fig. 14. Average spin magnitude $\langle I \rangle$ (solid lines) and average aligned component $\langle I_z \rangle$ (dashed lines) as a function of Q-value. For each system, the various symbols correspond to the two deep-inelastic fragments.

The differences in the alignment of each fragment may be understood in terms of the extracted individual spins and the dependence of the calculated spin fluctuations on different parameters[8,24]). The equiliberium statistical model predicts that the variances of the spin distributions are proportional to the temperature (eq. (9)). In addition, it also predicts that the variances decrease with increasing mass asymmetry of the system, although this dependence is rather weak throughout the region investigated in these experiments. In this mass-asymmetry region the variances along the three cartesian coordinates are nearly equal and the average value is larger for the heavy fragment. Finally, for a fixed mass asymmetry the magnitude of the fluctuations in both nuclei vary with the total mass according to the following relation:

$$\sigma^2 \propto A_{\text{total}}^{5/3}. \tag{20}$$

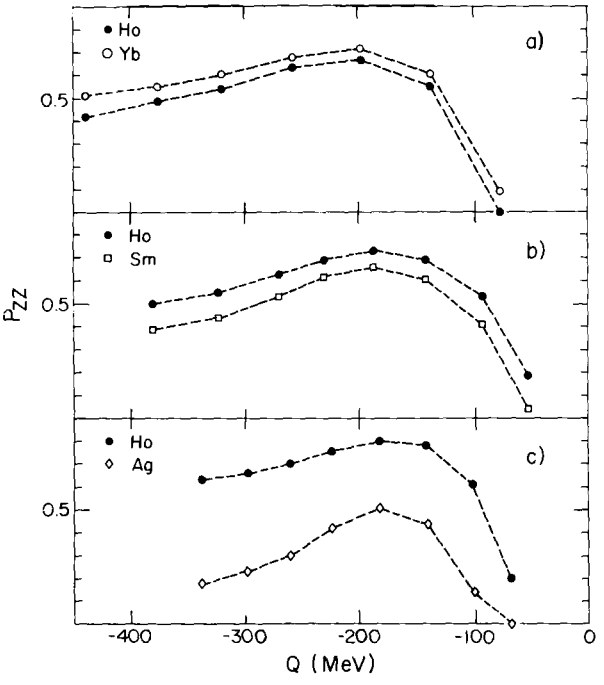

Fig. 15. Alignment parameter P_{zz} as a function of Q-value, for each of the two deep-inelastic fragments in the three reactions.

Table 2 summarizes the values of the calculated variance (as defined in eqs. (9) and (15)) associated with the spin distribution of each fragment. Due to the opposite effects derived from the increasing mass asymmetry and the decreasing total mass, the magnitude of the fluctuations induced in the Ho-like fragment is almost constant for the three reactions. Since the spin imparted to this nucleus increases with entrance-channel mass asymmetry, the net result is that the maximum value of P_{zz} (Ho) (fig. 15) increases with decreasing mass of the target (0.64, 0.72, and 0.79 for ^{176}Yb, ^{148}Sm, and ^{nat}Ag).

A different behavior is obtained for the extracted alignment of the target-like

TABLE 2

Calculated variances of the spin distributions (see eqs. (9) and (15))

Reaction	$\sigma^2/T(\hbar^2/\text{MeV})$	
	projectile (Ho)	target
^{165}Ho + ^{176}Yb	69.3	76.9
^{165}Ho + ^{148}Sm	69.0	57.9
^{165}Ho + ^{nat}Ag	68.5	34.5

nuclei. Although the calculated variances become smaller for lighter targets (table 2), the trend is not strong enough to compensate the dramatic decrease in the transferred spins (fig. 14). In fact, for the lightest nucleus (Ag) at the lowest excitation energies ($Q \simeq -300$ MeV), these randomly oriented components account for almost the totality of the spin (fig. 14c), thus giving rise to an almost isotropic spin distribution (fig. 15c). The measurement of discrete γ-rays appears as an interesting possibility to confirm these results on the alignment of each fragment.

6. Conclusions and summary

We have studied the spin-transfer process in the deep-inelastic reactions 1400 MeV ^{165}Ho + ^{176}Yb, ^{148}Sm and ^{nat}Ag, through the measurement of the multiplicity and anisotropy of continuum γ-rays. The total multiplicity conveys information on the sum of the spin magnitudes whereas the anisotropy of the angular distribution reflects the distribution of spin directions.

The experimental results were compared to a model that assumes complete relaxation of the rotational modes of the intermediate dinuclear complex. The validity of the equilibrium limit is suggested by the fact that the temperature dependence of the transferred spins is very similar in the three reaction systems, when expressed in units of the maximum angular momentum predicted by rigid rotation.

The two basic experimental inputs to the model calculation are the total γ-ray multiplicity and the multipolarity composition of the γ-ray spectra. Regarding the latter we have shown that, within reasonable limits prescribed by previous compound-nucleus work, the theoretical results do not depend crucially upon the assumptions made. As a final step we have calculated the primary spin distribution by taking into account the effects of neutron evaporation on the first and second moments. The agreement between the statistical model calculations and the experimental data is satisfactory throughout the entire Q-value range, although the depolarizing effect due to thermal fluctuations seems to be overestimated at the highest excitation energies ($Q \approx -100$ MeV).

The parameters (both extracted and calculated) of the spin distribution for each fragment in the different reactions were analyzed as a function of Q-value. In general, the spin magnitude and alignment increase across the quasielastic region. At smaller Q-values the spin magnitude almost saturates, while the alignment peaks and then falls for the most inelastic events. The alignment of the heavy reaction partner increases slightly with increasing mass asymmetry. On the other hand, although the fluctuations generated in the light fragment decrease with the mass, they account for a large fraction of the spin and therefore give rise to a substantial misalignment.

In summary, the study of the γ-ray decay from the heavy products of deep-inelastic reactions is a useful tool for the investigation of angular-momentum-transfer processes in moderately asymmetric systems. Comparisons between the data and a model calculation indicate that thermal equilibrium of the rotational degrees of freedom of the dinuclear complex is attained in a broad range of excitation energies and that the equilibrium limit is a natural starting point in the study of more complex phenomena associated with angular-momentum transfer in heavy ion reactions.

This work was supported by the Director, Office of Energy Research, Division of Nuclear Physics of the Office of High Energy and Nuclear Physics and by Nuclear Sciences of the Basic Energy Sciences Program of the US Department of Energy under Contract DE-AC03-76SF00098.

References

1) M. Lefort and C. Ngô, Riv. Nuovo Cim. **2**, No. **12** (1979) 1; and references therein
2) R. Babinet, B. Cauvin, J. Girard, J. M. Alexander, T. H. Chiang, J. Galin, B. Gatty, D. Guerreau and X. Tarrago, Z. Phys. **A295** (1980) 153
3) W. Kühn, R. Albrecht, H. Damjantschitsch, H. Ho, R. M. Ronningen, J. Slemmer, J. P. Wurm, I. Rode and F. Scheibling, Z. Phys. **A298** (1980) 95
4) L. G. Sobotka, C. C. Hsu, G. J. Wozniak, D. J. Morrissey and L. G. Moretto, Nucl. Phys. **A371** (1981) 510
5) P. Dyer, T. J. Haigh, R. Vandenbosch, T. D. Thomas, M. S. Zisman and L. Nunnelley, Nucl. Phys. **A322** (1979) 205
6) D. v. Harrach, P. Glässel, Y. Civelekoglu, R. Manner and H. J. Specht, Phys. Rev. Lett. **42** (1979) 1728
7) P. J. Haigh, P. Dyer, R. Vandenbosch, T. D. Thomas, L. Nunnelley and M. S. Zisman, Phys. Lett. **86B** (1979) 24
8) D. J. Morrissey, G. J. Wozniak, L. G. Sobotka, A. J. Pacheco, C. C. Hsu, R. J. McDonald and L. G. Moretto, Z. Phys. **305** (1982) 131
9) C. Le Brun, J. F. Lecolley, F. Lefebvres, M. L'Haridon, A. Osmont, J. P. Patry, J. C. Steckmeyer, R. Caroschik and F. Guilbault, Phys. Rev. **C25** (1982) 3212
10) R. Albrecht, W. Dünnweber, G. Graw, H. Ho, S. G. Steadman and J. P. Wurm, Phys. Rev. Lett. **34** (1975) 1400
11) P. Glässel, R. S. Simon, R. M. Diamond, R. C. Jared, I. Y. Lee, L. G. Moretto, J. O. Newton, R. Schmitt and F. S. Stephens, Phys. Rev. Lett. **38** (1977) 331
12) M. M. Aleonard, G. J. Wozniak, P. Glässel, M. A. Deleplanque, R. M. Diamond, L. G. Moretto, R. Schmitt and F. S. Stephens, Phys. Rev. Lett. **40** (1978) 622
13) Y. Eyal, H. Sann, D. Pelte, Y. Eyal, A. Gobbi, W. Kohl, U. Lynen, G. Rudolf, H. Stelzer and R. Bock, Phys. Rev. Lett. **41** (1978) 688
14) F. Gerschel, M. A. Deleplanque, M. Ishihara, C. Ngô, N. Perrin, J. Péter, B. Tamain, L. Valentin, D. Paya, Y. Sugiyama, M. Berlanger and F. Hanappe, Nucl. Phys. **A317** (1979) 473
15) M. N. Namboodiri, J. B. Natowitz, P. Kasiraj, R. Eggers, L. Adler, P. Gonthier, C. Cerruti and S. Simon, Phys. Rev. **C20** (1979) 982
16) P. R. Christensen, F. Folkmann, O. Hansen, O. Nathan, N. Trautner, F. Videbaek, S. Y. Van Der Werf, H. C. Britt, P. P. Chestnut, H. Freiesleben and F. Pühlhofer, Nucl. Phys. **A349** (1980) 217
17) R. A. Dayras, R. G. Stokstad, D. C. Hensley, M. L. Halbert, D. G. Sarantites, L. Westerberg and J. H. Barker, Phys. Rev. **C22** (1980) 1485

18) K. Van Bibber, R. Ledoux, S. G. Steadman, F. Videbaek, G. Young and C. Flaum, Phys. Rev. Lett. **38** (1977) 334
19) C. Lauterbach, W. Dünnweber, G. Graw, W. Hering, H. Puchta and W. Trautmann, Phys. Rev. Lett. **41** (1978) 1774
20) H. Puchta, W. Dünnweber, W. Hering, C. Lauterbach and W. Trautmann, Phys. Rev. Lett. **43** (1979) 623
21) R. J. Puigh, H. Doubre, A. Lazzarini, A. Seamster, R. Vandenbosch, M. S. Zisman and T. D. Thomas, Nucl. Phys. **A336** (1980) 279
22) R. J. McDonald, A. J. Pacheco, G. J. Wozniak, H. H. Bolotin, L. G. Moretto, C. Shück, S. Shih, R. M. Diamond and F. S. Stephens, Nucl. Phys. **A373** (1982) 54
23) L. G. Moretto and R. P. Schmitt, Phys. Rev. **C21** (1980) 204
24) R. P. Schmitt and A. J. Pacheco, Nucl. Phys. **A379** (1982) 313
25) F. S. Stephens, Lawrence Berkeley Laboratory report LBL-10356, published in Proc. Varenna Conf., Varenna, Italy, July 1979
26) L. C. Northcliffe and R. F. Schilling, Nucl. Data Tables **A7** (1970) 233
27) J. B. Moulton, J. E. Stephenson, R. P. Schmitt and G. J. Wozniak, Nucl. Instr. **157** (1978) 325
28) T. K. Alexander and J. S. Forster, Advances in nuclear physics, vol. 10 (Plenum, New York, 1978) ch. 3
29) R. S. Simon, M. V. Banaschik, P. Colombani, D. P. Soroka, F. S. Stephens and R. M. Diamond, Phys. Rev. Lett. **36** (1976) 359
30) L. Westerberg, D. G. Sarantites, K. Geoffrey, R. A. Dayras, J. R. Beene, M. L. Halbert, D. C. Hensley and J. H. Barker, Phys. Rev. Lett. **41** (1978) 96
31) S. J. Feenstra, J. Van Klinken, J. P. Pijn, R. Janssens, C. Michel, J. Steyaert, J. Vervier, K. Cornelis, M. Huyse, and G. Lhersonneau, Phys. Lett. **80B** (1979) 183
32) S. R. de Groot, H. A. Tolhoek, and W. J. Huiskamp, Alpha-, beta and gamma-ray spectroscopy, ed. K. Siegbahn, vol. 2 (North-Holland, Amsterdam, 1966)
33) R. Nordhagen, G. Goldring, R. M. Diamond, K. Nakai and F. S. Stephens, Nucl. Phys. **A142** (1970) 577
34) D. G. Sarantites, J. H. Barker, M. L. Halbert, D. C. Hensley, R. A. Dayras, E. Eichler, N. R. Johnson and S. A. Gronemeyer, Phys. Rev. **C14** (1976) 2138
35) W. U. Schröder and J. R. Huizenga, Ann. Rev. Nucl. Sci. **27** (1977) 465; and references therein
36) L. G. Moretto and R. P. Schmitt, J. de Phys. **37** (1976) C5-109; and references therein
37) G. Wolschin, Nucl. Phys. **A316** (1979) 146
38) R. Vandenbosch, Phys. Rev. **C20** (1979) 171
39) H. Esbensen, A. Winther, R. A. Broglia and C. H. Dasso, Phys. Rev. Lett. **41** (1978) 296
40) L. G. Moretto, Lawrence Berkeley Laboratory Report LBL-12596
41) S. K. Blau and L. G. Moretto, Nucl. Phys. **A359** (1981) 477
42) L. G. Moretto, S. K. Blau and A. J. Pacheco, Nucl. Phys. **A364** (1981) 125
43) R. M. Diamond and F. S. Stephens, Annual Review of Nuclear and Particle Science **30** (1980) 85, Annual Review, Inc., Palo Alto, CA; and references therein
44) S. H. Sie, J. O. Newton and R. M. Diamond, Nucl. Phys. **A367** (1981) 176
45) M. A. Deleplanque, Th. Byrski, R. M. Diamond, H. Hübel, F. S. Stephens, B. Herskind and R. Bauer, Phys. Rev. Lett. **41** (1978) 1105